Optimum orientation of compact and elongated hexadecapole deformed actinide targets: Application to synthesizing superheavy nuclei

Harshit Sharma [1,*] Shivani Jain,[2,†] Raj Kumar [1,‡] and Manoj K. Sharma[1,§]

[1]*School of Physics and Materials Science, Thapar Institute of Engineering & Technology, Patiala 147004, Punjab, India*

[2]*Key Laboratory of Frontiers in Theoretical Physics, Institute of Theoretical Physics, Chinese Academy of Sciences, Beijing 100190, China*

(Received 4 August 2023; revised 14 September 2023; accepted 2 October 2023; published 24 October 2023)

Background: The quadrupole ($\beta_2^{\pm}$) deformed targets in the actinide region are found to be of great relevance in the production of superheavy nuclei (SHN), in both the hot and cold fusion mechanisms. Recently, the application of "elongated or cold" and "compact or hot" configurations of pear-shape octupole (up to $\beta_3^{\pm}$) deformed nuclei was found to play significant role in the fusion-fission dynamics of heavy-ion induced reactions, in the low energy regime.

Purpose: To understand the relevance of higher-order deformed (up to $\beta_4^{\pm}$) actinides and their compact and elongated nuclear fusion configurations in the production cross section of SHN, we have obtained the optimum orientations ($\theta_{\rm opt}$) in reference to the above mentioned configurations of β_4-deformed targets. For this, a variety of projectile-target combinations—spherical (^{36}S, ^{40,48}Ca) and $\beta_2^{\pm}$-deformed (^{30}Si, ^{34}S) nuclei as incident beams and β_4-deformed (with different signs $\pm$ and magnitudes) actinides ($\approx$1400 isotopes) as targets—are taken into consideration. Later, the application of $\theta_{\rm opt}^{\rm hot/cold}$ ($\beta_2^{\pm}\beta_3^{\pm}\beta_4^{\pm}$) was done to analyze the fragmentation structure of ^{286}Cn*.

Methods: On the basis of the proximity theorem, the optimum orientations ($\theta_{\rm opt}$) defining the compact and elongated configurations of deformed nuclei are obtained at the maximum and minimum barrier height, respectively. Further, the obtained $\theta_{\rm opt}$ and static deformations (up to $\beta_4^{\pm}$) for around 1400 isotopes of actinides are utilized in the calculations of capture cross section $\sigma_{\rm cap}(E_{\rm c.m.})$ using the extended ℓ-summed Wong model at energies lying across the Coulomb barrier. Also, to study the fragmentation structure of ^{286}Cn* SHN, the collective clusterization approach of quantum mechanical fragmentation theory has been adopted.

Results: For a large variety of projectile-target combinations, leading to SHN, the incorporation of higher-order deformation (up to $\beta_4^{\pm}$) shows a significant influence on $\theta_{\rm opt}^{\rm hot/cold}$ with the effect of $\pm$ signs and different magnitudes of $\beta_4^{\pm}$ deformation. Also, with the incorporation of deformations up to $\beta_4^{\pm}$ and corresponding $\theta_{\rm opt}$, the $\sigma_{\rm cap}(E_{\rm c.m.})$ improves and is in better agreement with the available experimental data of ^{238}U-based reactions, across the barrier energies. Also, in the decay channel, the β_4-deformed fragments, i.e., ^{143}Ba + ^{143}Ba, are found to minimize the fragmentation potential, as compared to the β_2 or β_3 deformed fragments.

Conclusion: The present study concludes that the optimized configurations of higher-order deformed actinides up to β_4 participate relatively better than the optimized configurations of β_2 and β_3 deformed nuclei in the formation as well as exit channel of superheavy nuclei.

DOI: 10.1103/PhysRevC.108.044613

I. INTRODUCTION

The criterion of choosing the appropriate projectile-target (P-T) combination for the formation of the compound nucleus (CN) of superheavy nuclei (SHN) (atomic number $Z \geqslant 104$), has attracted prodigious attention in the field of low-energy nuclear reactions. Although the production of such a superheavy element is a very difficult task, researchers have found heavy-ion (mass $\geqslant$4 and charge $\geqslant$2) induced reactions to be the most relevant probe for studying the nuclear fusion mechanisms leading to SHN [1–5]. The main intent of synthesizing superheavy nuclei is to extend the periodic table and reach toward the 'Island of Stability," which defines the most stable stage of nuclei for magic numbers $Z = 114, 120, 126$ and $N = 162, 184$ [6,7].

To date, numerous experiments have been performed to synthesize SHN. The successful production of SHN has become possible via two different nuclear fusion mechanisms, named cold and hot fusion reactions [8,9]. In the former case, a stable target of lead-208 (^{208}Pb) or bismuth-209 (^{209}Bi) is bombarded with suitable projectiles, leading to the formation of a CN ($Z = 104$–112) with an excitation energy $E_{\rm CN}^*$ lying in the range 10–20 MeV [10]. On the other hand, in the hot fusion mechanism, neutron-rich projectiles like ^{48}Ca are used to hit highly deformed actinide targets and subsequently form CN ($Z = 112$–118) with $E_{\rm CN}^* = 30$–45 MeV [11–18].

*hsharma.nph@gmail.com
†jain.shivani@itp.ac.cn
‡rajkumar@thapar.edu
§msharma@thapar.edu

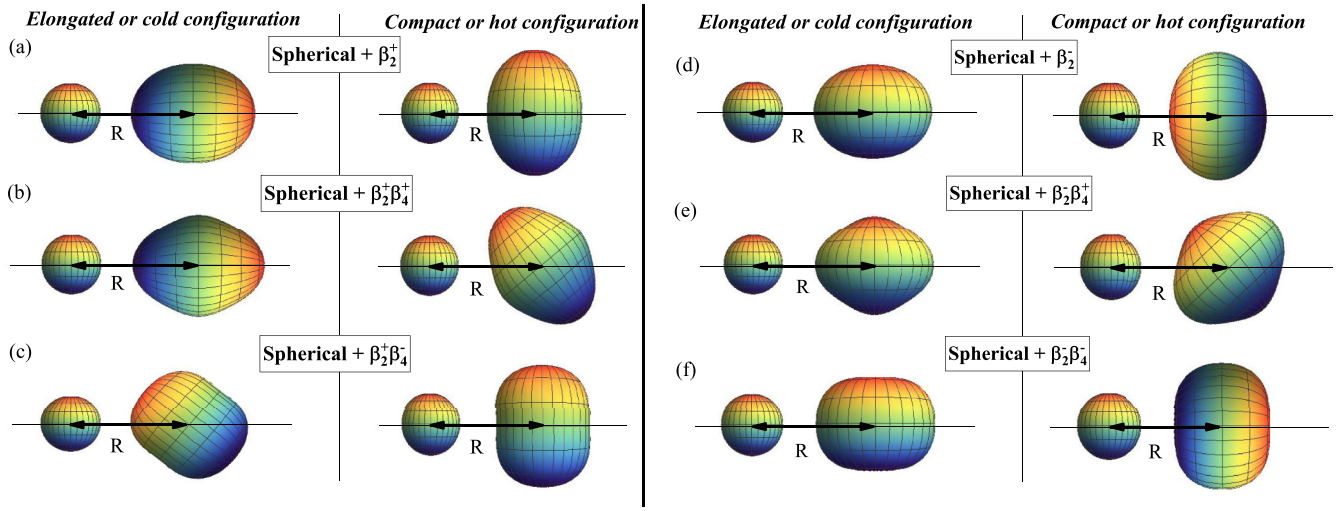

FIG. 1. Schematic diagram of elongated (or cold) and compact (or hot) fusion configurations for spherical (Sph) + (a) β_2^+, (b) $\beta_2^+\beta_4^+$, (c) $\beta_2^+\beta_4^-$, (d) β_2^-, (e) $\beta_2^-\beta_4^+$, and (f) $\beta_2^-\beta_4^-$ projectile-target combinations. Note that the magnitudes of quadrupole (β_2) and hexadecapole deformations (β_4) are 0.236 and 0.098, respectively, of the ^{238}U target nucleus, and ^{48}Ca is taken as projectile nucleus of spherical shape.

Besides, theoreticians, through their rigorous efforts, have found that the collision between deformed and oriented nuclei participates significantly in the production of stable and long-lived nuclei. In the early 1980s, it was found that the gentle fusion among two similar nuclei, e.g., ^{238}U, could lead to a long-lived giant molecule [19]. Based on such analysis, theoreticians have performed numerous calculations and analyzed the effect of deformation and orientation degrees of freedom on the fusion barrier and fusion cross section. For an illustration, the elongated (pole-to-pole) configuration of prolate quadrupole (β_2^+) deformed similar nuclei lowers the fusion barrier and subsequently enhances the reaction cross sections. On the other hand, the belly-to-belly configuration of quadrupole deformed nuclei increases the fusion barrier, reducing the cross section [20]. In other words, on the basis of these configurations, researchers have explored the relevance of deformation and orientation degree of freedom in heavy-ion induced fusion reactions for incident beam energies lying across the Coulomb barrier [21–37].

The above discussion raises a relevant question that up to which order should the deformations be considered to provide the relevant details of cross sections, especially for CN of the superheavy region ($Z = 104$–118)? In the search of an answer, researchers initially analyzed the impact of hexadecapole (β_4) deformations on the fusion barrier and fragmentation structure of SHN formed via hot fusion ^{48}Ca-induced reactions [38]. Later, in [32], the authors found that with the inclusion of β_4-deformation the evaporation residue (ER) cross sections get improved for the hot fusion reactions. Besides, the importance of belly-to-belly and tip-to-tip collision, respectively, for both the hot (^{48}Ca + ^{238}U) and cold fusion (^{70}Zn + ^{208}Pb) reactions has been studied across the Coulomb barrier energies [14]. However, such analysis is broadly done for the quadrupole deformation of the deformed colliding nuclear partners. Note that, in the present work, the word "optimum" refers to [24], where it is used to define the orientation corresponding to the elongated and compact configurations having minimal and maximum barrier heights respectively. However, in [39], the authors optimized the orientation to identify the best possible projectile-target combinations for synthesizing superheavy nuclei.

In the present work, we intend to explore the importance of respective optimum orientations ($\theta_{\rm opt}$) of higher-order deformation (up to β_4), which help in defining the "elongated or cold" and "compact or hot" configurations of deformed nuclei, in the fusion as well as decay of superheavy compound nuclei. The relevance of $\theta_{\rm opt}$ obtained in reference to the aforementioned configurations of β_4-deformed nuclei is tested for incident energies lying across the Coulomb barrier. For the above analysis, it is quite important to comprehend the effect of $+/-$ signs and magnitude of deformations up to β_4 on $\theta_{\rm opt}$, which is further compared with $\theta_{\rm opt}$ obtained with the inclusion of quadrupole $\beta_2^{\pm}$ [28] and octupole $\beta_3^{\pm}$ deformations [40].

In the present work, we have opted for around 1400 hexadecapole deformed actinides as targets, bombarded with ^{30}Si, ^{34,36}S, ^{40,48}Ca projectiles. For an illustration, in Fig. 1 we show a schematic diagram of the elongated (or cold) and compact (or hot) configurations of deformed ^{238}U ($\beta_2^{\pm} = \pm 0.236$, $\beta_3^{\pm} = 0$, and $\beta_4^{\pm} = \pm 0.098$) target which is hit by spherical projectile ^{48}Ca. From this figure, one may estimate the change in the separation distance R between the centers of two colliding nuclei, as one goes from the spherical + quadrupole (β_2^+ and β_2^-) deformed case towards the spherical + hexadecapole ($\beta_2^{\pm}\beta_4^{\pm}$) case. A significant change in the nuclear shape with the effect of higher-order deformation (up to $\beta_4^{\pm}$) from that of $\beta_2^{\pm}$ shape modifies R. Such observations motivate us to analyze the corresponding effects on the fusion barrier characteristics and, consequently, on the fusion cross sections over a wide range of incident beam energies.

In the present calculations, we first investigated the change in $\theta_{\rm opt}$ with the incorporation of $\beta_4^{\pm}$ along with $\beta_2^{\pm}$ deformations for the considered isotopes. Then the essence of octupole deformation present in some actinides was also accounted for

along with the $\beta_2^{\pm}$ and $\beta_4^{\pm}$ deformations. Further, as an application of $\theta_{\rm opt}$, we calculated the capture cross sections ($\sigma_{\rm cap}$) with the use of the extended ℓ-summed Wong model, for ^{238}U-based reactions with cross sections at fixed optimum orientations as well as cross sections integrated over all orientations ($\sigma_{\rm Int}$) and compared the results with the available experimental data [41–45] over a wide range of incident energies. We also explore the relevance of $\theta_{\rm opt}$ obtained with the incorporation of higher-order deformation (up to β_4) in the exit channel of SHN using the collective clusterization approach of the quantum mechanical fragmentation theory (QMFT) [46–48]. In the present work, the fragmentation potential has been extended with the inclusion of higher-order deformations up to β_4 along with the relative optimum orientations, $\theta_{\rm opt}$, defining the elongated and compact configurations of the decay fragments.

This paper is organized as follows to carry forward with the above idea. In Sec. II the formalism of the extended ℓ-summed Wong model, the contributing potentials, and the fragmentation theory of QMFT, used to pursue the present analysis, are summarized. In Sec. III the results and observations of the present analysis are discussed, followed by a summary of the work in Sec. IV.

II. METHODOLOGY

The shape of the deformed nuclear surface can be expressed through the radius vector $R_i(\alpha_i)$, which involves the spherical harmonics $Y_\lambda^{(0)}(\alpha_i)$ of higher order, i.e., $\lambda = 2, 3, 4$ [49–52], as given by

$$R_i(\alpha_i) = R_{0i}\left[1 + \sum_{\lambda=2,3,4}\beta_{\lambda i}Y_{\lambda i}^{(0)}(\alpha_i)\right] = R_{0i}\left[1 + \sum_{\lambda=2,3,4}\beta_{\lambda i}\sqrt{\frac{2\lambda+1}{4\pi}}P_\lambda(\cos\alpha_i)\right], \quad (1)$$

where $i = 1, 2$ correspond to projectile and target nuclei, respectively. $R_{0i}(=1.28A_i^{1/3} - 0.76 + 0.8A_i^{-1/3})$ in fm [53] represents the radius of the equivalent spherical nuclei. $\beta_{\lambda i}$ is the static deformation parameter taken from the data table of Möller *et al.* [52]. $\lambda = 2, 3, 4$ defines the quadrupole, octupole, and hexadecapole deformed shapes, respectively. $P_\lambda(\cos\alpha_i)$ are the Legendre polynomials. The detail of angles can be found in [20]. The above radius term is involved as input in the total interaction potential and its constituent terms, as discussed below.

A. Total interaction potential

To study heavy-ion induced reactions in the low-energy regime, the total interaction potential $V_T(R)$ is considered an important tool, and is defined as the combination of Coulomb potential $V_C(R)$, centrifugal potential $V_\ell(R)$, and nuclear potential $V_N(R)$. The deformations (up to β_4) and relative orientations (θ_i) of deformed nuclei are incorporated in these contributing potentials. Thus, the total potential $V_T(R, A_i, \beta_{\lambda i}, \theta_i)$ is defined as

$$V_T(R, A_i, \beta_{\lambda i}, \theta_i) = V_C(R, Z_i, \beta_{\lambda i}, \theta_i) + V_\ell(R, A_i, \beta_{\lambda i}, \theta_i) + V_N(R, A_i, \beta_{\lambda i}, \theta_i), \quad (2)$$

where the Coulomb potential $V_C(R, Z_i, \beta_{\lambda i}, \theta_i)$ for deformed-deformed pairs of colliding nuclei is defined as

$$V_C(R) = \frac{Z_1Z_2e^2}{R} + Z_1Z_2e^2\sum_{\lambda=2,3,4}^{i=1,2}\left(\frac{R_i^\lambda(\alpha_i)}{R^{\lambda+1}}\right)\beta_\lambda Y_\lambda^{(0)}(\theta_i) \times\left[\frac{3}{2\lambda+1} + \left(\frac{12}{7(2\lambda+1)}\right)\beta_\lambda Y_\lambda^{(0)}(\theta_i)\right]. \quad (3)$$

It is important to note that, for spherical projectiles, the second term of the above equation will have terms only for $i = 2$, i.e., deformed target, as $\beta_{21} = 0.0$ and $\beta_{22} \neq 0.0$. The centrifugal potential $V_\ell(R, A_i, \beta_{\lambda i}, \theta_i)$ is in the form of rotational kinetic energy and is given as

$$V_\ell(R, A_i, \beta_{\lambda i}, \theta_i) = \frac{\hbar^2\ell(\ell+1)}{2I}, \quad I = \mu R^2. \quad (4)$$

In Eq. (2), the nucleus-nucleus interaction potential $V_N(R, A_i, \beta_{\lambda i}, \theta_i)$ is defined on the basis of the "proximity theorem," given by Blocki and his collaborators [53] as the product of $4\pi\bar{R}\gamma b$, which is a function of the shape and geometry of the colliding nuclei, and $\Phi(s_0)$, a universal function depending on the shortest distance between the interacting nuclei [53–55]. Thus, $V_N(R, A_i, \beta_{\lambda i}, \theta_i)$ is given as

$$V_N(R, A_i, \beta_{\lambda i}, \theta_i) = 4\pi\bar{R}\gamma b\Phi(s_0), \quad (5)$$

where s_0 is the minimum separation distance between the two facing surfaces of interacting nuclei. $\bar{R}$ is the mean curvature radius expressed in terms of the radii of curvatures R_{i1} and R_{i2} for coplanar nuclei as [53]

$$\frac{1}{\bar{R}^2} = \frac{1}{R_{11}R_{12}} + \frac{1}{R_{21}R_{22}} + \frac{1}{R_{11}R_{22}} + \frac{1}{R_{21}R_{12}}. \quad (6)$$

The principal radii of curvature (R_{i1} and R_{i2}) for spherical-deformed and deformed-deformed cases is given [56] as

$$R_{i1}(\alpha_i) = \frac{\left[R_i^2(\alpha_i) + R_i'^2(\alpha_i)\right]^{3/2}}{R_i^2(\alpha_i) + 2R_i'^2(\alpha_i) - R_i(\alpha_i)R_i''(\alpha_i)}, \quad R_{i2}(\alpha_i) = \frac{R_i(\alpha_i)\sin\alpha_i}{\cos(\pi/2 - \alpha_i - \delta_i)}. \quad (7)$$

It is important to note, for spherical projectiles, $R_{11(\alpha_1)} = R_{12}(\alpha_1) = R_1(\alpha_1)$. In Eq. (5) [53], γ is the surface energy constant and is expressed for axially symmetric terms as

$$\gamma = 0.9517\left[1 - 1.7826\left(\frac{N-Z}{A}\right)^2\right]\ \text{MeV fm}^{-2}., \quad (8)$$

b is the surface thickness, having value 0.99 fm.

In Eq. (5), the universal function with single parameter s_0 is given as

$$\Phi(s_0) = \begin{cases} -\frac{1}{2}(s_0 - 2.54)^2 - 0.0852(s_0 - 2.54)^3, & s_0 \leqslant 1.2511\ \text{fm}, \\ -3.437\exp\left(-\frac{s_0}{0.75}\right), & s_0 > 1.2511\ \text{fm}. \end{cases} \quad (9)$$

From Eqs. (2)–(9), defining the total interaction potential, one can get the details of fusion barrier characteristics, i.e., barrier height V_B, barrier position R_B, and barrier curvature $\hbar\omega_B$, which are influenced by the effects of deformation and orientation degrees of freedom. These terms are further utilized in the calculations of capture cross sections.

B. Capture cross sections, $\sigma_{\rm cap}(E_{\rm c.m.}, \theta_i)$

The capture cross section, in terms of angular momentum (ℓ) partial waves, for deformed and oriented nuclei, lying in the same planes and colliding with center-of-mass energy $E_{\rm c.m.}$, is defined using the extended ℓ-summed Wong formula of the one-dimensional penetration model [54] as

$$\sigma_{\rm cap}(E_{\rm c.m.}, \theta_i) = \sum_{\ell=0}^{\infty} \sigma_\ell = \frac{\pi}{k^2} \sum_{\ell=0}^{\infty} (2\ell+1) P_\ell, \tag{10}$$

with $k = \sqrt{\frac{2\mu E_{\rm c.m.}}{\hbar^2}}$ and μ as the reduced mass. P_ℓ is the transmission coefficient for each ℓ, which describes the penetration probability across the Coulomb barrier. Here, $\ell_{\rm max}$ is the maximum angular momentum calculated using the sharp cutoff approximation [54,57,58].

In the present work, the penetration probability P_ℓ was obtained using the Hill-Wheeler [59] and Wentzel-Kramers-Brillouin (WKB) approximations [60], defined as

$$P_\ell^{\rm HW}(E_{\rm c.m.}) = \left[1 + \exp\left(\frac{2\pi\left[V_B^\ell(E_{\rm c.m.}) - E_{\rm c.m.}\right]}{\hbar\omega_\ell(E_{\rm c.m.})}\right)\right]^{-1} \tag{11}$$

and

$$P_\ell^{\rm WKB}(E_{\rm c.m.}) = \exp\left[-\frac{2}{\hbar}\int_{R_a}^{R_b}\left\{2\mu\left[V_B^\ell(E_{\rm c.m.}) - Q_{\rm eff}\right]\right\}^{1/2} dR\right], \tag{12}$$

respectively.

In Eq. (11), $V_B^\ell(E_{\rm c.m.})$, $R_B^\ell(E_{\rm c.m.})$, and $\hbar\omega_B^\ell(E_{\rm c.m.})$ represent the barrier height, barrier position, and barrier curvature, respectively, which are extracted from the total interaction potential V_T [61]. On the other hand, in Eq. (12), $Q_{\rm eff}$ [$=V(R_a)$] is the effective Q value of the entrance channel. R_a and R_b are the two turning points; for reference see Fig. 1 of [62]. $R_a = R_1(\alpha_1) + R_2(\alpha_2) + \Delta R$, where ΔR is the neck-length parameter, which is introduced to define the tunneling path. The permissible value of ΔR lies in the nuclear proximity range of about 2 fm, since the surface interaction between the colliding nuclei can take place around this range. Further, to observe the effect of hexadecapole deformation over all the orientations, the fusion cross sections are integrated over θ_2 for the spherical + deformed combination, as given by

$$\sigma_{\rm Int}(E_{\rm c.m.}) = \int_{\theta_i=0}^{\pi/2} \sigma(E_{\rm c.m.}, \theta_i) \sin\theta_1 d\theta_1 \sin\theta_2 d\theta_2. \tag{13}$$

C. The fragmentation theory for deformed and oriented nuclei

The fragmentation analysis is worked out in terms of the mass asymmetry parameter (i.e., $\eta_A = \frac{|A_1 - A_2|}{A_1 + A_2}$), the relative separation distance R, the neck parameter ϵ, deformations $\beta_{\lambda i}$ ($\lambda = 2, 3, 4$ correspond to quadrupole, octupole, and hexadecapole deformations, respectively), and orientation θ_i degrees of freedom. Here, $i = 1, 2$ stand respectively for fragments 1 and 2 [63,64]. In terms of these parameters, the fragmentation potential $V(\eta, R)$ is the sum of binding energies and the $\beta_{\lambda i}$ and θ_i dependent Coulomb, proximity, and centrifugal potentials of decaying fragments, as given by

$$V(\eta, R) = -\sum_{i=1}^{2} B_i(A_i, Z_i, \beta_{\lambda i}) + V_C(R, Z_i, \beta_{\lambda i}, \theta_i) + V_N(R, A_i, \beta_{\lambda i}, \theta_i) + V_\ell(R, A_i, \beta_{\lambda i}, \theta_i). \tag{14}$$

Here, the binding energy $B_i(A_i, Z_i, T)$ [$=V_{\rm LDM}(A_i, Z_i, T) + \delta U_i \exp(-T^2/T_0^2)$] of a nucleus at temperature T is defined on the basis of the Strutinsky renormalization procedure [65]. The $V_{\rm LDM}$ considered is from the temperature-dependent liquid drop model (LDM) of Davidson *et al.* [66]. For relevant details see Ref. [67]. The second term, i.e., shell-corrections δU, is given by Myers and Swiatecki [65] with its T dependence from Davidson *et al.* [66]. The term T represents the temperature and is obtained using the statistical relation [68] $E^*_{\rm CN} = \frac{A_{\rm CN}}{a} T^2 - T$. Here the level density parameter $a = 12$ for superheavy nuclei [69].

The formalism related to the contributing potentials, that is, Coulomb, nuclear, and centrifugal potentials, used in the above equation of fragmentation potential was discussed above in Eq. (3), (4), and (5).

III. RESULTS AND DISCUSSION

In the process of obtaining the optimum orientations ($\theta_{\rm opt}$) which define the "elongated or cold" and "compact or hot" configurations of higher-order deformed (up to hexadecapole β_4 deformation) actinides, we have considered a large variety of projectile-target (P-T) combinations. In these combinations, spherical (^{36}S and ^{40,48}Ca) and quadrupole deformed (^{30}Si and ^{34}S) nuclei are used as projectiles, and around 1400 actinides with different magnitude and signs of β_2, β_3, and β_4 deformation are taken as targets. The above analysis is discussed in reference to that of quadrupole $\beta_2^\pm$ and octupole $\beta_3^\pm$ deformations[1] for both the cold and hot fusion configurations. Later on, the application of $\theta_{\rm opt}^{\rm hot/cold}$ obtained with the effect of $\beta_2^\pm$, $\beta_3^\pm$, and $\beta_4^\pm$ deformation is analyzed in terms of the fragmentation structure of the superheavy nucleus.

Before going into a comprehensive study, initially we worked on some ^{238}U-based nuclear reactions and calculated capture cross sections [$\sigma_{\rm cap}(E_{\rm c.m.})$] with the incorporation of deformation (up to β_4) and corresponding $\theta_{\rm opt}$. The related discussion on to the above analysis is given in the following section.

[1] In the Möller data table of deformations [52], only negative values of β_3 deformation are given. Thus, in the present work, the results are for $\beta_2^\pm \beta_3^- \beta_4^\pm$ shape.

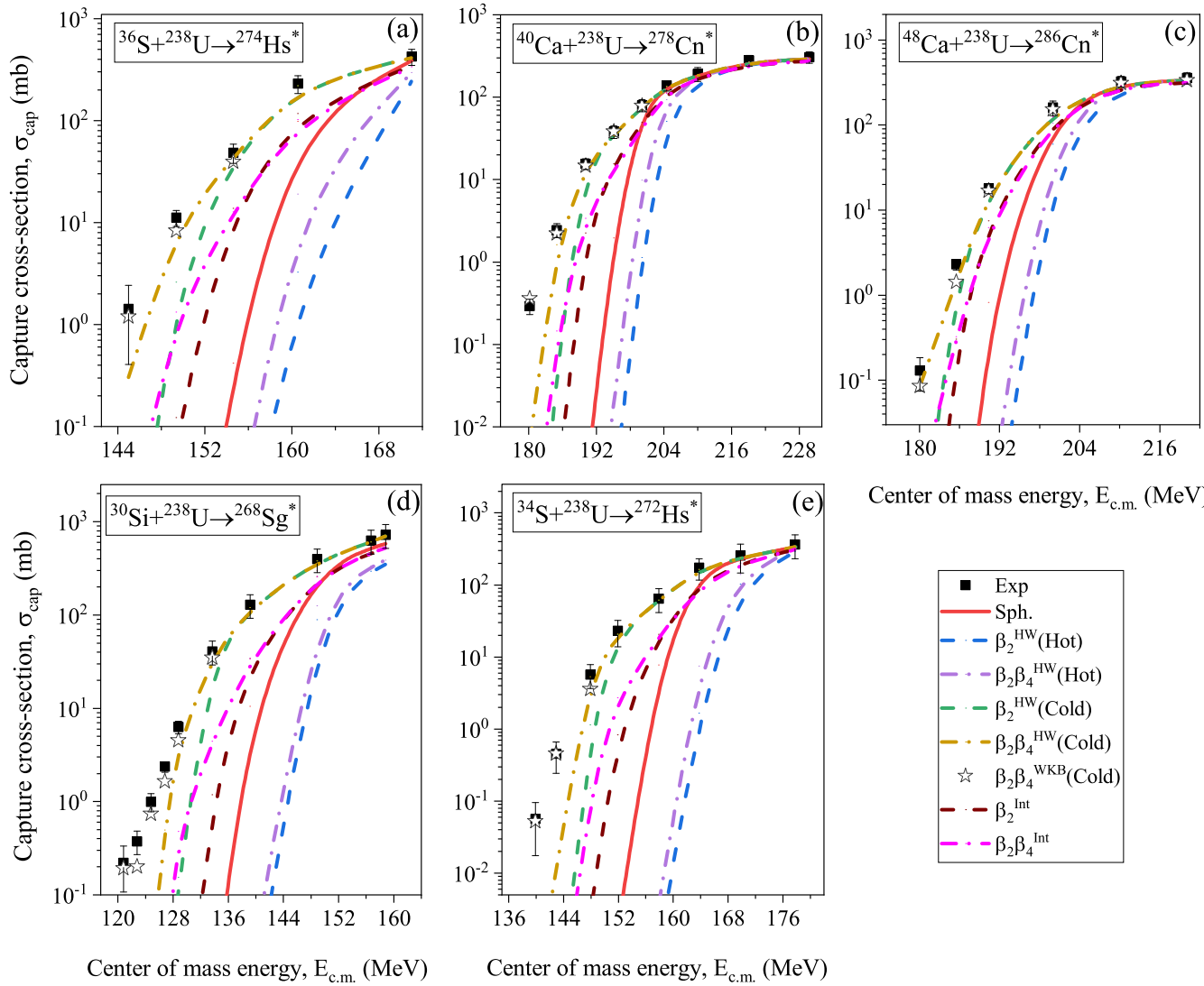

FIG. 2. The capture cross sections (σ_{cap}) and cross sections integrated over possible orientations (σ_{Int}) are calculated using the extended ℓ-summed Wong model [54] for ^{238}U-based reactions as a function of $E_{c.m.}$. The calculated σ_{cap} and σ_{Int} for considered choices of projectile-target combinations are compared with the available experimental data for incident energies lying across the Coulomb barrier.

A. Capture cross sections of ^{238}U-based reactions

We calculated the capture cross sections (σ_{cap}), using the extended ℓ-summed Wong model [54], with respect to the center-of-mass energy ($E_{c.m.}$) for ^{30}Si, ^{34,36}S, ^{40,48}Ca + ^{238}U projectile-target combinations. For each reaction, $\sigma_{cap}(E_{c.m.})$ is calculated in three steps: (I) $\beta_{2i}^{\pm} = \beta_{4i}^{\pm} = 0.0$ (here $i = 1, 2$ labeled for projectile and target nuclei, respectively), i.e., spherical case, (II) $\beta_{2i}^{\pm} \neq 0.0$ and $\beta_{4i}^{\pm} = 0.0$, quadrupole deformed case, and (III) $\beta_{2i}^{\pm} \neq 0.0$, $\beta_{4i}^{\pm} = 0.0$ and $\beta_{42}^{\pm} \neq 0.0$, hexadecapole deformed case (as for ^{238}U $\beta_3 = 0.0$), as shown in Fig. 2. It is important to mention that the choice of θ_{opt}, for the respective elongated and compact configurations, is made on the basis of the order of deformation ($\lambda = 2, 4$ of β_λ). In Table I, we have listed the values of deformation β_{2i}, β_{4i} and related optimum orientations θ_i of colliding nuclear partners. In Fig. 2, the calculated $\sigma_{cap}(E_{c.m.})$ for all the above mentioned cases are compared with the available experimental data [43–45,70]. With this comparison, we have determined that the cross sections improve as one moves from hot configuration to spherical to cold configuration of β_{42} deformation, which is reflected in the targets of ^{30}Si and ^{34,36}S, ^{40,48}Ca-

TABLE I. The quadrupole (β_{2i}) and hexadecapole (β_{4i}) deformations of colliding nuclear partners. Note that here the projectile nuclei are either spherical or quadrupole deformed.

				Elongated		Compact	
Reaction	$\beta_{21}^{\pm}$	$\beta_{22}^{\pm}$	$\beta_{42}^{\pm}$	θ_1	θ_2	θ_1	θ_2
$^{36}S + ^{238}U$	0.00	0.236	0.098	0°	70°	0°	180°
$^{40}Ca + ^{238}U$	0.00	0.236	0.098	0°	72°	0°	180°
$^{48}Ca + ^{238}U$	0.00	0.236	0.098	0°	75°	0°	180°
$^{30}Si + ^{238}U$	−0.236	0.236	0.098	0°	76°	90°	180°
$^{34}S + ^{238}U$	−0.235	0.236	0.098	0°	72°	90°	180°

induced reactions, especially at the below- and near-barrier energies. However, there is still some hindrance observed in $\sigma_{cap}(\beta_2\beta_4)$ (cold) from σ_{cap}^{Expt}, mainly in the sub-barrier region. Note that, in order to observe the average effect of orientation degree of freedom, the integrated cross sections over all mutual orientations of the deformed nuclei are also shown in Fig. 2.

As noted, for the calculation of σ_{cap} we used the extended ℓ-summed Wong model [see Eq. (10)], which is expressed in terms of quantum-mechanical transmission/penetration probability, P_ℓ. This term defines the penetration of the barrier by the projectile (with some kinetic energy), to hit and fuse into the target for an equilibrated formation of CN. The above discussed results are based on the Hill-Wheeler approximation [see Eq. (11)], used to calculate P_ℓ. According to this approximation, P_ℓ is dependent on V_B, R_B, and $\hbar\omega_B$, which gives larger area of penetration under the inverted Harmonic oscillator curve. Consequently, the hindrance is noticed in the below barrier region. To overcome this problem, we have opted to use another approximation, i.e., the WKB approach [see Eq. (12)] in which the penetration path is decided on the basis of neck-length parameter ΔR [60]. It was also noticed in Ref. [71] that the WKB approach gives better results, especially for the below-barrier region. The permissible values of this parameter lie in the nuclear proximity range of about 2 fm, since the surface interaction between two colliding partners can take place around this range of ΔR. In reference to the experimental data of considered choices of ^{238}U-based nuclear reactions, we have noticed a systematic trend in the neck-length parameter depending on the mass number of the compound nucleus, A_{CN}, and the kind of projectile beam; for reference see Fig. 3. In this figure, we show the variation of ΔR (fm), with respect to A_{CN}, separately for spherical (^{36}S, ^{40}Ca, and ^{48}Ca) and quadrupole deformed (^{30}Si and ^{34}S) projectile beams. Here, its value increases with the decrease in the mass of projectile, which is from either a spherical or quadrupole deformed beam. This value of ΔR remains constant for independent choice of beam energy of each reaction and supports addressing the experimental data of ^{238}U-based reactions.

It is important to mention here that the calculations done so far are for $\beta_{22}^{+}\beta_{42}^{+}$ deformed shape of the target nucleus. As in our recent work [20], we have defined all the possible geometries of a hexadecapole deformed nucleus with different signs on β_2 and β_4 deformation, viz., $\beta_2^{+}\beta_4^{+}$, $\beta_2^{-}\beta_4^{+}$, $\beta_2^{+}\beta_4^{-}$, and $\beta_2^{-}\beta_4^{-}$. In the present work, we also tested the effect of $+/-$ signs of β_4 deformation on the fusion barrier of reactions leading to the formation of SHN. For an illustration, we have plotted the total interaction potential V_T (MeV) as a function of separation distance R (fm) for ^{48}Ca ($\beta_{21} = \beta_{41} = 0.0$) + ^{238}U ($\beta_{22} = \pm 0.236$, $\beta_{42} = \pm 0.098$), as shown in Fig. 4. As we know, to study heavy-ion induced reactions the total potential, considered as an important tool, provides the barrier characteristics (barrier height V_B, barrier position R_B, and barrier curvature $\hbar\omega_B$), which are very sensitive to the deformation and orientation degree of freedom. In Fig. 4, one may notice that, with the inclusion of deformation up to β_4, there is a significant modification of the barrier in reference to that of the spherical case. For the positive value of β_4 [see panels (a) and (c) of Fig. 4], the barrier gets lower than that of the β_2 case for both the cold and hot configurations. In contrast to this, the negative sign of β_4 deformation increases the barrier from that of β_2; see panels (b) and (d) of Fig. 4. Such modifications observed on the barrier with the effect of different signs of β_4 deformation would definitely influence the cross sections for incident energies lying across the Coulomb barrier. Besides, we are also interested in investigating the effect of magnitude, along with different signs of higher-order deformations (β_2, β_3, and β_4) of all the deformed targets belonging to the actinide region, on the optimum orientations of elongated and compact configurations. The highly deformed actinides are generally considered as targets in collision with ^{48}Ca or neighboring nuclei for the successful formation of superheavy nuclei. The related discussion is provided in detail in the following section.

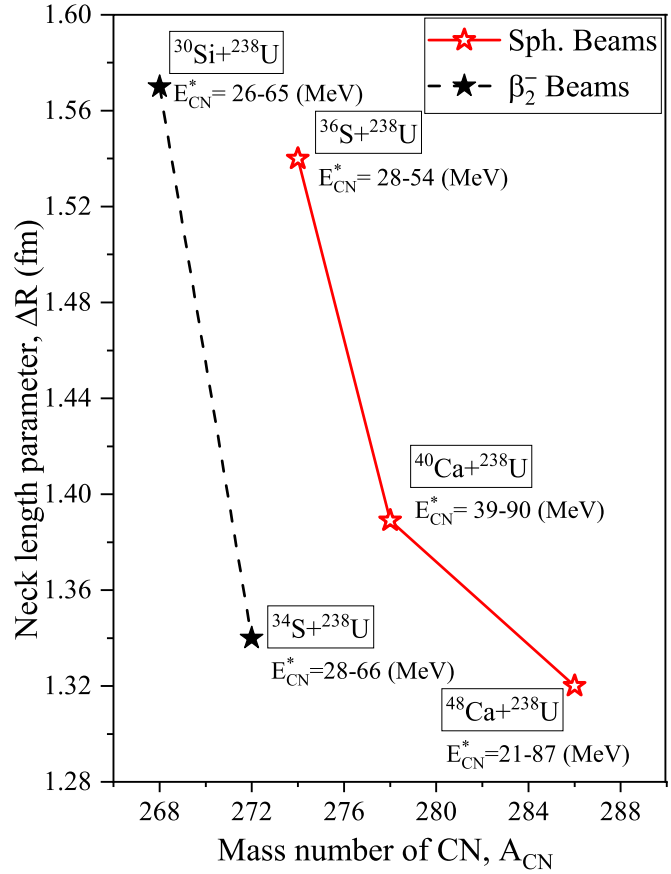

FIG. 3. Variation of neck length parameter ΔR (fm) is shown as a function of mass number A_{CN} of CN for ^{238}U-based reactions, with spherical (open star) and β_2^- deformed (closed star) projectile beams.

B. Optimum orientations corresponding to elongated and compact configurations of hexadecapole deformed actinide targets

In the preceding section, we analyzed the relevance of optimum orientations (θ_{opt}) defining the elongated (or cold) and compact (or hot) configuration of hexadecapole and

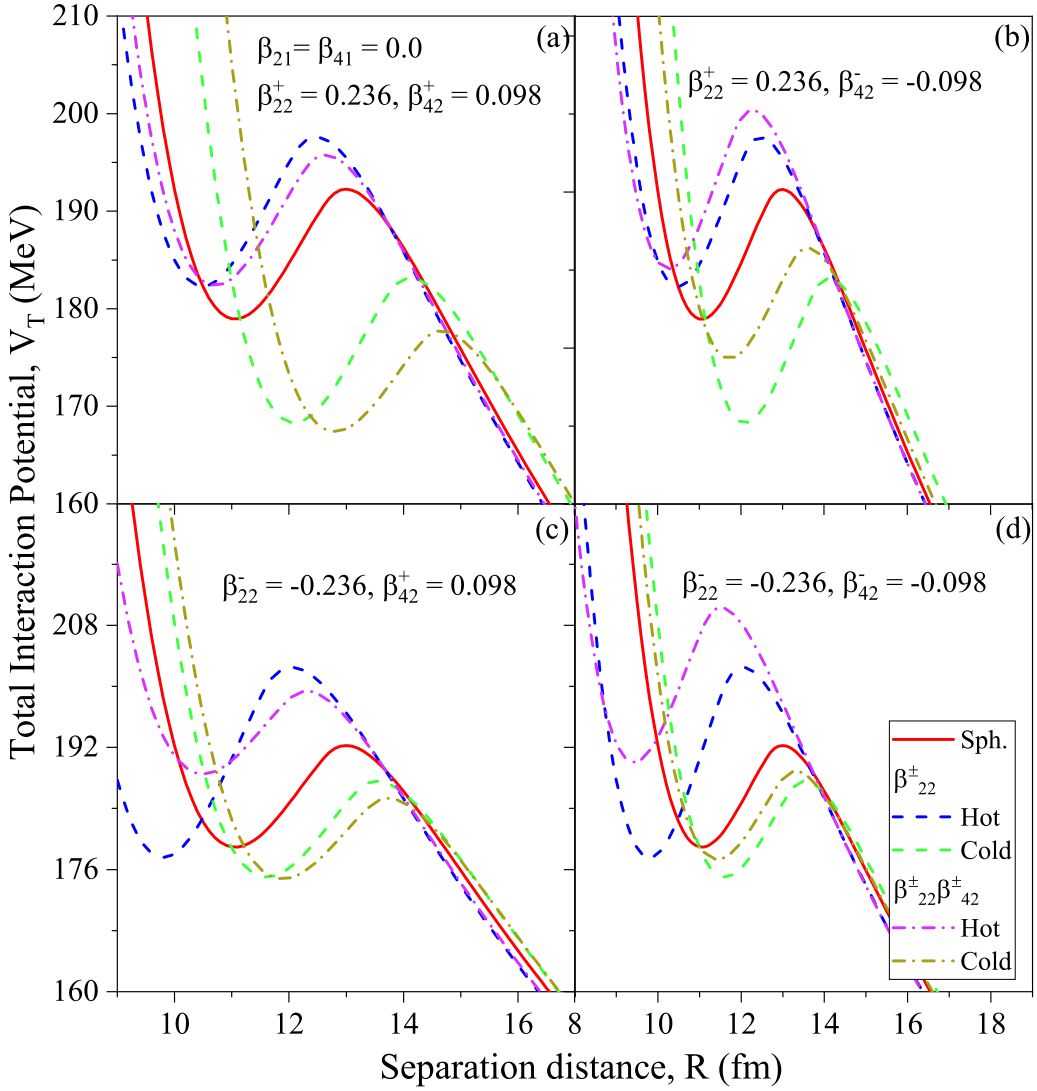

FIG. 4. Total interaction potential V_T (MeV) is plotted as a function of separation distance R (fm) for ^{48}Ca ($\beta_{21} = \beta_{41} = 0.0$) + ^{238}U ($\beta_{22} = 0.236$, $\beta_{42} = 0.098$) for different combinations of $\beta_2^{\pm}$ and $\beta_4^{\pm}$. (a) $\beta_{22}^{+} = 0.236$, $\beta_{42}^{+} = 0.098$, (b) $\beta_{22}^{+} = 0.236$, $\beta_{42}^{-} = -0.098$, (c) $\beta_{22}^{-} = -0.236$, $\beta_{42}^{+} = 0.098$, and (d) $\beta_{22}^{-} = -0.236$, $\beta_{42}^{-} = -0.098$.

quadrupole deformed nuclei in the calculation of capture cross sections for incident beam energies lying across the Coulomb barrier. From this analysis, we found out that the optimized orientation for the elongated and compact configurations of $\beta_2^{\pm}\beta_4^{+}$ deformed nuclei shows better agreement with the experimental results as compared to the optimum orientations of β_2 deformed nuclei for ^{238}U-based reactions. This is because, due to positive value of β_4 deformation, the Coulomb barrier gets lower than in the $\beta_2^{\pm}$ case.

In this section, we consider around 1400 hexadecapole deformed actinides ($90 \leqslant Z \leqslant 103$) as targets bombarded with ^{30}Si, ^{34}Ti, and ^{48}Ca projectiles. Note that these deformed nuclei have different magnitudes and signs of deformations (up to β_4), and subsequently show corresponding effects on $\theta_{\rm opt}$. For an illustration, the change in optimum orientation [i.e., $\theta_{\rm opt}(\beta_2^{\pm}) - \theta_{\rm opt}(\beta_4^{\pm})$] and magnitude of $\beta_4^{\pm}$ deformation are shown with respect to the mass number of all the deformed isotopes of the thorium compound nucleus; see Fig. 5. This figure is categorized in four panels for (a) $\beta_2^{+}\beta_4^{+}$, (b) $\beta_2^{-}\beta_4^{+}$, (c) $\beta_2^{+}\beta_4^{-}$, and (d) $\beta_2^{-}\beta_4^{-}$ nuclei with $\beta_3^{\pm} = 0$ for these cases. Due to positive and negative values of β_4 deformation, one may notice the change in $\theta_{\rm opt}(\beta_2^{\pm}) - \theta_{\rm opt}(\beta_4^{\pm})$ for the "compact or hot" and "elongated or cold" configurations, respectively. A significant change in optimum orientation observed is for those isotopes which have relatively higher magnitude of $\beta_4^{\pm}$ than $\beta_2^{\pm}$. The trend followed by $\theta_{\rm opt}(\beta_2^{\pm}) - \theta_{\rm opt}(\beta_4^{\pm})$ is in accordance with that of the magnitude of $\beta_4^{\pm}$. So, one can clearly state that a significant change in optimum angles with the effect of larger value of $|\beta_4^{\pm}|$ will be noticed on the fusion barrier and subsequently on the fusion cross sections.

Further, in Figs. 6–9, we show $\theta_{\rm opt}(\beta_2^{\pm}) - \theta_{\rm opt}(\beta_4^{\pm})$ for all the actinide ($90 \leqslant Z \leqslant 103$) isotopes having only quadrupole and hexadecapole deformation with respect to the magnitude

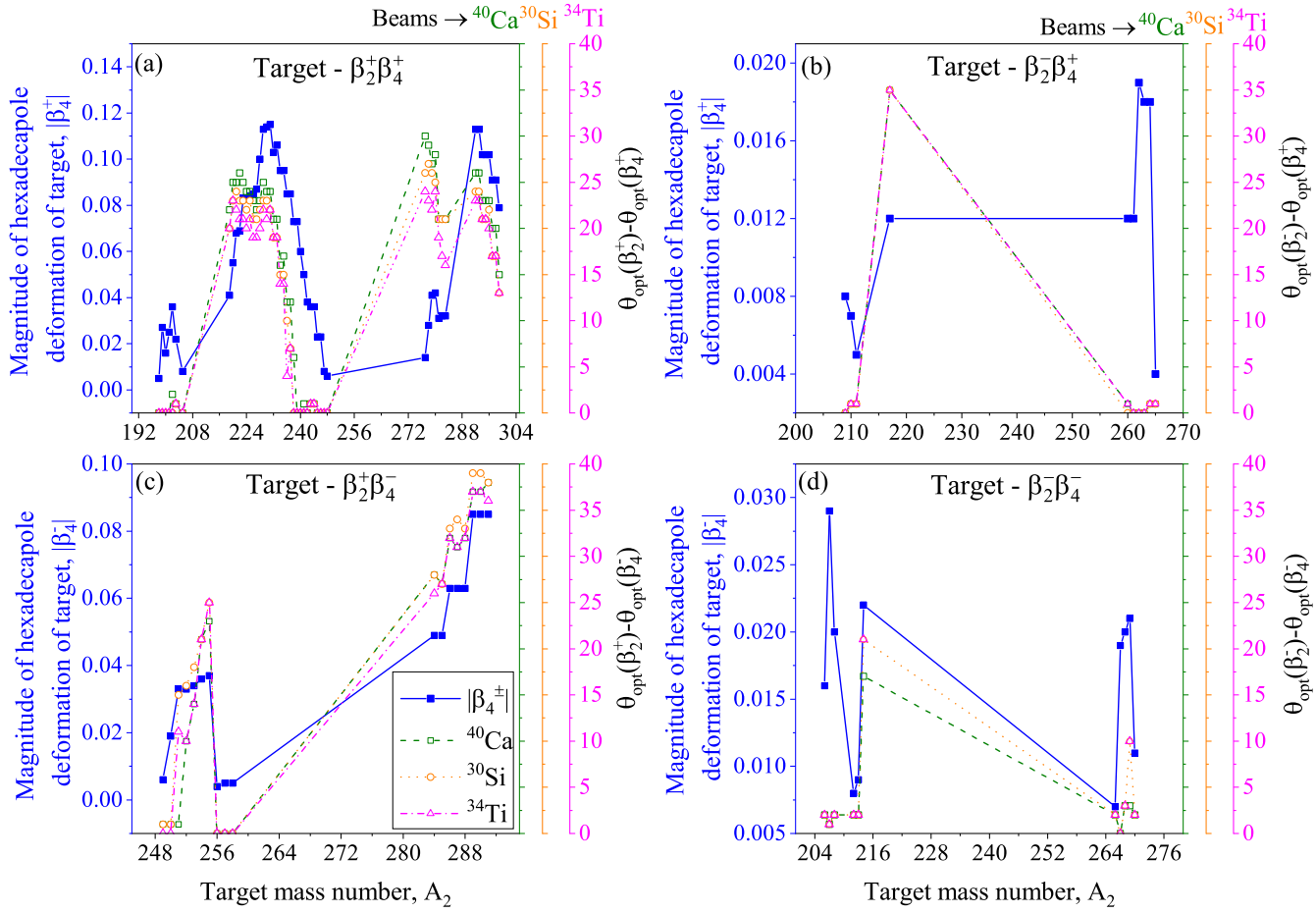

FIG. 5. The change in the magnitude of hexadecapole deformation ($|\beta_4^{\pm}|$) and optimum orientation $\theta_{opt}(\beta_2^{\pm}) - \theta_{opt}(\beta_4^{\pm})$ is shown with respect to the mass number of Th isotopes, which are categorized as (a) $\beta_2^+\beta_4^+$, (b) $\beta_2^-\beta_4^+$, (c) $\beta_2^+\beta_4^-$, and (d) $\beta_2^-\beta_4^-$. Note that this analysis is done for ^{30}Si, ^{48}Ca, and ^{34}Ti + ^{A_2}Th projectile-target combinations.

of β_4. In these figures, the difference in the magnitudes of β_2 and β_4 deformations is categorized in eight ranges, which are specified with different symbols and colors. From these figures, the maximum change in $\theta_{opt}(\beta_2^{\pm}) - \theta_{opt}(\beta_4^{\pm})$ is observed for higher magnitude of β_4 deformation, only when the difference between magnitudes of β_2 and β_4 comes within the range of 0–0.05 and also for higher magnitude of β_4 ($\geqslant$0.040). Besides, it is important to acknowledge the role of octupole deformation (β_3) which break the symmetry of the nuclear shape around the reflection axis [72]. In a recent study [40,62], three of us investigated the relevance of pear shape of octupole deformed (up to β_3) nuclei in the fusion as well as fission dynamics of heavy-ion induced reactions. In the present work, we have opted for deformations up to β_4, apart from the actinides used in the discussion of Figs. 6–9, where some isotopes possess quadrupole, octupole, as well as hexadecapole deformations; for reference, see the data table of static deformations in [52]. So for these we have noticed modifications in θ_{opt} of hot (or compact) configuration. For convenience, we have given in Table II $\theta_{opt}(\beta_2^{\pm}\beta_3^{\pm}\beta_4^{\pm})$ for both the soft ($|\beta_3| < |\beta_2|$ and β_4) and rigid pear-shape ($|\beta_3| \geqslant |\beta_2|$ and β_4) nuclei. This result holds true for all the actinides belonging to the $90 \leqslant Z \leqslant 103$ region, with a few exceptional cases. These exceptional results are because of very small values of β_3 and β_4 deformations. Besides, we have observed approximately 5% change in both the barrier height V_B as well as barrier position R_B, due to incorporation of higher-order deformation (up to β_4) and θ_{opt} from Table II, compared to the spherical case. It is important to mention that, for the cold configuration, there is no change in θ_{opt} as one goes from β_2 to β_3 to β_4, since the nuclear shape of higher-order deformation is being elongated in the same direction as in the quadrupole

TABLE II. Optimum orientations (θ_{opt}^{hot}) for the "compact or hot" configurations of actinides (belonging to $Z = 90$–103 region), in which quadrupole ($\beta_2^{\pm}$), octupole ($\beta_3^{\pm}$), and hexadecapole ($\beta_4^{\pm}$) deformations are nonzero.

Nuclear shape	Optimum orientation θ_{opt}^{hot}
Soft pear shape ($\|\beta_3^{\pm}\| < \|\beta_2^{\pm}\|$)	$65^\circ \pm 3^\circ$
Rigid pear shape ($\|\beta_3^{\pm}\| \geqslant \|\beta_2^{\pm}\|$)	I: $65^\circ \pm 3^\circ$ if $\|\beta_4^{\pm}\| \geqslant 0.04$ II: $180^\circ \pm 3^\circ$ if $\|\beta_4^{\pm}\| < 0.04$

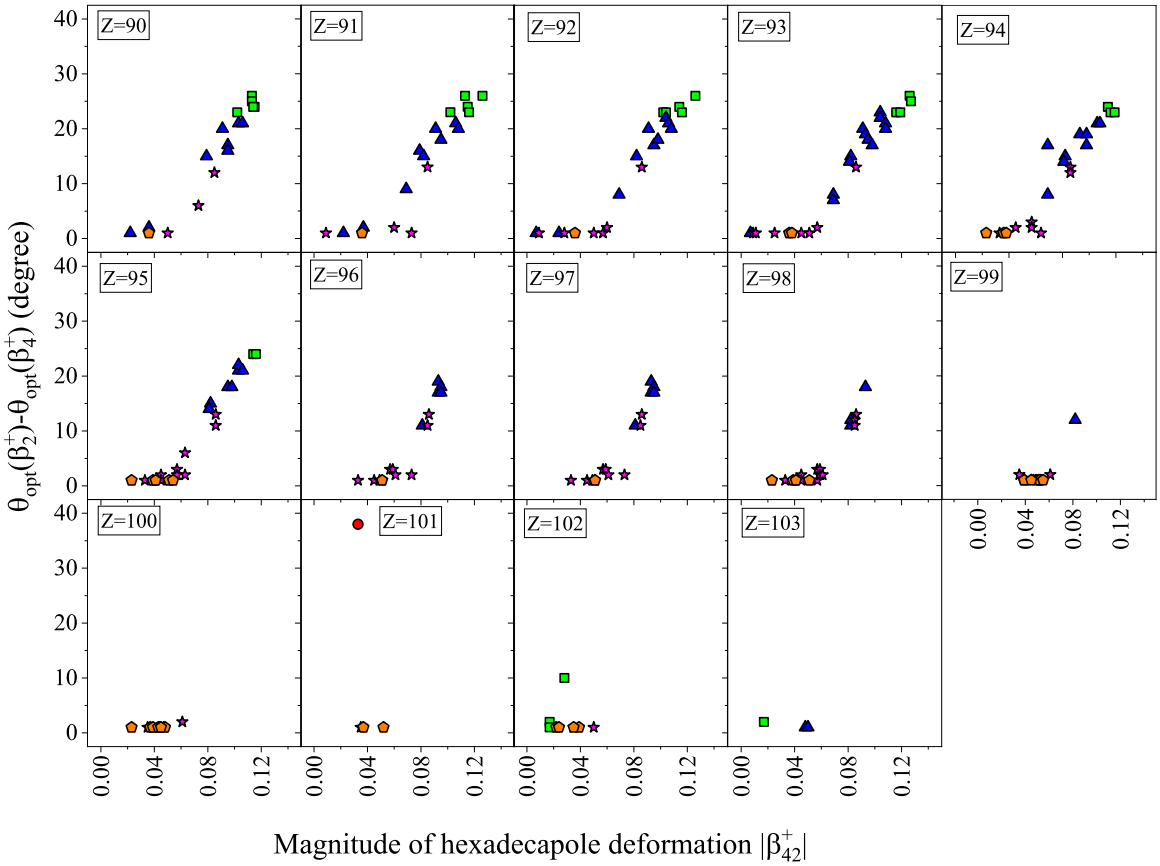

FIG. 6. The difference between $\theta_{\rm opt}(\beta_2^+)$ and $\theta_{\rm opt}(\beta_4^+)$ is shown with respect to the magnitude of hexadecapole deformation β_{42}^+ of the actinide targets ($90 \leqslant Z \leqslant 103$). Note that, due to positive value of β_{42}, the change in $\theta_{\rm opt}$ is observed for the "compact" or "hot" fusion configuration.

shape. However, due to elongation in the shape, one may notice the change of ≈10% in the barrier characteristics from those of the spherical case.

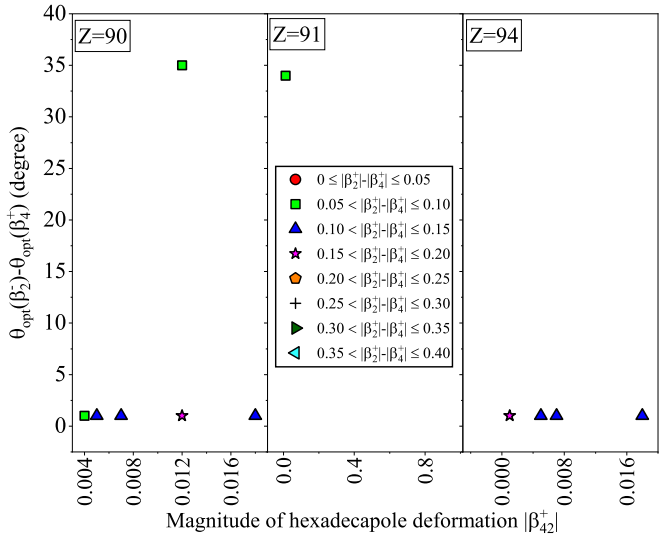

FIG. 7. Same as Fig. 6, but for the $\beta_2^- \beta_4^+$ case.

From the above analysis, it can be said that the "+" and "−' signs of β_4 deformation show changes in $\theta_{\rm opt}$ of hot and cold configurations, respectively. So far, we have gathered the details of $\theta_{\rm opt}$ with the effect of higher-order deformation (up to β_4) and its different signs for a large variety of entrance channels, which are leading toward the formation of superheavy nuclei. Further, it would be interesting to analyze the application of $\theta_{\rm opt}(\beta_4^{\pm})$ in the exit channel of SHN.

C. Application of $\beta_{4i}^{\pm}$ and respective $\theta_{\rm opt}(\beta_{4i}^{\pm})$ in the fission region

Finally, in the subsection, we intend to make the application of the optimum orientations ($\theta_{\rm opt}$) obtained for the "elongated or cold" and "compact or hot" configurations of higher order deformed (up to $\beta_4^{\pm}$) nuclei in the exit channel of the formed compound nuclear system. In view of this, the fragmentation theory based on the collective clusterization approach of quantum mechanical fragmentation theory (QMFT) has been chosen to understand the relevance of higher-order deformation and respective $\theta_{\rm opt}$ in the decay fragments. For illustration, in Fig. 10, we have plotted the fragmentation potential $V(\eta)$ (MeV) with respect to the fragment mass number A_2 (or $A_1 = A_{\rm CN} - A_2$; complementary fragment) of the decay of the ^{286}Cn* superheavy compound nucleus, formed via

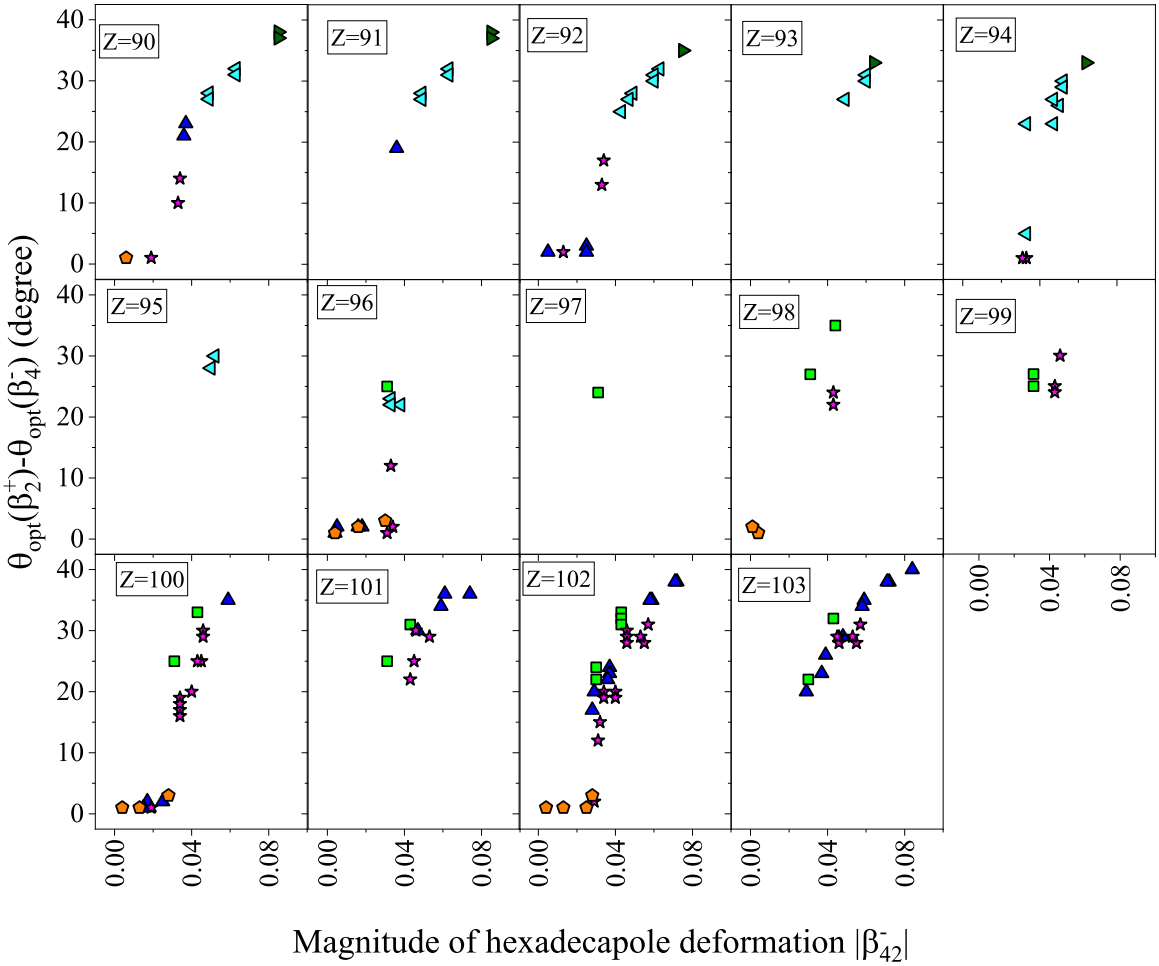

FIG. 8. Same as Fig. 6, but for the "elongated or cold" fusion configuration of $\beta_2^+\beta_4^-$ cases.

the $^{48}\mathrm{Ca}+^{238}\mathrm{U}$ projectile-target combination. This analysis was done at a common excitation energy $E^*_{\mathrm{CN}} = 21.7$ MeV, angular momentum $\ell = 0\hbar$, and fixed neck-length parameter $\Delta R = 1.30$ fm. Note that ΔR is chosen in reference to the addressing of experimental data of capture cross section for the $^{48}\mathrm{Ca}+^{238}\mathrm{U}$ reaction at $E_{\mathrm{c.m.}} = 180.1$ MeV (or excitation energy $E^*_{\mathrm{CN}} = 21.7$ MeV) in the preceding section. For reference, see Figs. 2 and 3. The deformations up to $\lambda = 4$ order and respective optimum orientations are taken into account, and comparison is made for the case of spherical fragments. It is important to mention that, to specifically analyze the influence of deformation and orientation degree of freedom, we obtained $V(\eta)$ at $\ell = 0\hbar$.

In Fig. 10, $V(\eta)$ is minimized initially by considering (I) the spherical case (i.e., $\beta_\lambda = 0$), (II) quadrupole ($\beta^\pm_{2i}$) deformation and $\theta_{\mathrm{opt}}(\beta^\pm_{2i})$, (III) octupole ($\beta^\pm_{3i}$) and $\theta_{\mathrm{opt}}(\beta^\pm_{2i}\beta^\pm_{3i})$, and (IV) hexadecapole (β_{4i}) and $\theta_{\mathrm{opt}}(\beta^\pm_{2i}\beta^\pm_{3i}\beta^\pm_{4i})$ introduced for all the possible decaying fragments from $^{286}\mathrm{Cn}^*$ CN. This analysis was done for both the cold and hot configurations of deformed fragments, but we show the results for the former in Fig. 10. With hot configurations, there is nominal change in the fragmentation structure irrespective of the choice of deformation and orientation degree of freedom. This is because the fragments of spherical shape give relatively larger radius than that of the hot configuration of deformed fragments. Consequently, the spherical shape fragments have more minima in $V(\eta)$.

On the other hand, in the fragmentation structure of the cold configuration (see Fig. 10), we have noticed the change in the fragmentation structure, as one goes from spherical to the higher-order deformation of possible decaying fragments from the $^{286}\mathrm{Cn}^*$ CN. The main change was observed in the heavy mass fragment (HMF) and fission valley, marked in Fig. 10. For these regions, the fragment mass belongs to the ranges $21 \leqslant A_2 < \frac{A_{\mathrm{CN}}}{2} - 35$ and $\frac{A_{\mathrm{CN}}}{2} - 35 \leqslant A_2 \leqslant \frac{A_{\mathrm{CN}}}{2}$, respectively. It is important to mention here that there is no change in the structure of $V(\eta)$ for evaporation residue (ER; $1 \leqslant A_2 \leqslant 4$) and intermediate mass fragment (IMF; $4 < A_2 <$ HMF region) regions, irrespective of choice of deformation order. In the HMF region, the fragments with minima in $V(\eta)$ obtained for spherical and octupole deformation cases are different from those of quadrupole and hexadecapole deformed cases. Due to incorporation of higher-order deformation and corresponding cold optimum orientation, $^{63}\mathrm{Mn}$ ($Z_1 = 25$, $N_1 = 38$) + $^{223}\mathrm{Fr}$ ($Z_2 = 87$, $N_2 = 136$) fragments are found to possess relatively deeper minima in $V(\eta)$. Here, one of the decaying partners possess deformed magicity in its neutron number (i.e., $N_1 = 38$) [73]. Such a study would

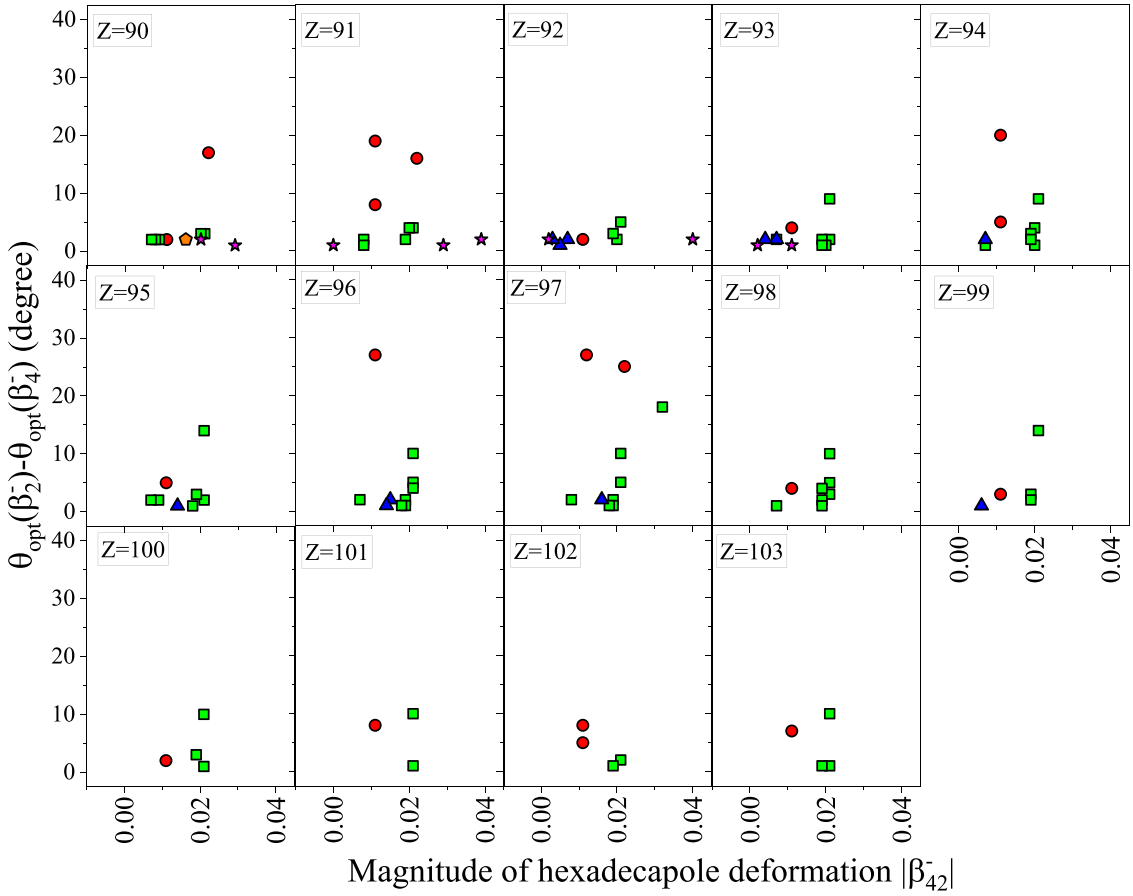

FIG. 9. Same as Fig. 6, but for the "elongated or cold" fusion configuration of $\beta_2^-\beta_4^-$ cases.

be helpful to understand the stability and deformed magicity, especially in the HMF region of SHN.

Further, in the fission region, for the spherical case we have analyzed that ^{152}Nd ($Z_1 = 60$, $N_1 = 92$) + ^{134}Te ($Z_2 = 52$, $N_2 = 82$) fragments possess the minimum value of $V(\eta)$ among the rest of the fission fragments. These are the near-symmetric fission fragments with $\eta_A(=\frac{|A_1-A_2|}{A_1+A_2}) = 0.063$, and one of them (i.e., ^{134}Te) has magicity in its neutron number, which imparts more stability to emit out of the compound nucleus. Further, with the inclusion of $\beta_{2i}^{\pm}$ and $\theta_{\rm opt}^{\rm cold}(\beta_{2i}^{\pm})$, ^{180}Yb ($Z_1 = 70$, $N_1 = 110$) + ^{106}Mo ($Z_2 = 42$, $N_2 = 64$) fragments with $\eta_A = 0.259$ are found to have minima in $V(\eta)$. Also note that one of the decaying partners (^{106}Mo) has deformed magicity [73], due to which the fragmentation potential minimizes compared to that of spherical nuclei. This result holds true as we introduce octupole deformation $\beta_{3i}^{\pm}$ and respective cold optimum orientation $\theta_{\rm opt}^{\rm cold}(\beta_{2i}^{\pm}\beta_{3i}^{\pm})$. However, with the inclusion of higher-order deformation up to β_4 and respective $\theta_{\rm opt}$, one may notice a significant change in the fragmentation structure of the fission valley. For this situation, we have analyzed that ^{143}Ba ($Z_1 = 56$, $N_1 = 87$) + ^{143}Ba ($Z_2 = 56$, $N_2 = 87$) symmetric fragments ($\eta_A = 0.0$) appear across minima in $V(\eta)$. In a recent experimental [74] and theoretical work [62], the authors analyzed that a fragment with atomic number = 56 and neutron number = 88, or in its vicinity, possesses extra stability compared to spherical and quadrupole deformed nuclei. This result has been observed in the asymmetric fission of compound nuclei belonging to the actinide region. In the present work, we have observed the fragments in the symmetric fission region of a superheavy compound nucleus, i.e., ^{286}Cn*.

The above analysis is an open problem of understanding the role of hexadecapole deformation and respective optimum orientation in the exit channel of superheavy nuclei, at various extremities such as angular momentum, energy/temperature, etc.

IV. SUMMARY

In the present work, we have obtained the optimum orientations ($\theta_{\rm opt}$) of higher-order deformed (up to hexadecapole β_4 deformation) targets and analyzed their relevance on the fusion barrier and fusion cross section. These $\theta_{\rm opt}$ define the "elongated or cold" and "compact or hot" configurations of deformed nuclei and help to address the nuclear properties across the Coulomb barrier.

In the above analysis, we have seen that $\theta_{\rm opt}$ obtained with the strong effect of $\beta_4^{\pm}$ deformation shows significant change from that of lower-order deformation, i.e., octupole $\beta_3^{\pm}$ and quadrupole $\beta_2^{\pm}$, on the barrier characteristics. The

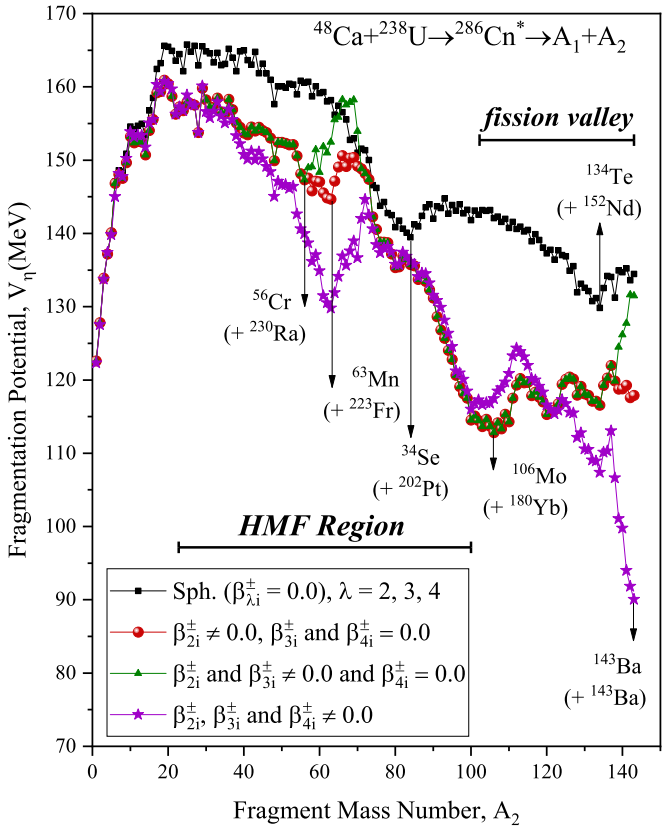

FIG. 10. The minimized fragmentation potential $V(\eta)$ (MeV) is shown as a function of fragment mass number A_2 (or $A_1 = A_{CN} - A_2$; complementary fragment) for the cold configurations of the possible decaying fragments, whose quadrupole $\beta^{\pm}_{2i}$, octupole $\beta^{\pm}_{3i}$, and hexadecapole deformations $\beta^{\pm}_{4i}$ along with their optimum orientations are introduced one by one in the calculation. Note that the above analysis is compared with the spherical case as well, at a common value of excitation energy E^*_{CN}, angular momentum $\ell = 0\hbar$, and neck-length parameter $\Delta R = 1.30$ fm.

above analysis has been tested for over 1400 actinide targets, bombarded with spherical (^{36}S, $^{40,48}Ca$) and quadrupole deformed (^{30}Si, ^{34}S) beams. The result obtained in the context of θ_{opt} is independent of the choice of incident energy. Besides, in comparison to the available experimental data of capture cross sections (σ_{cap}) for ^{238}U-based reactions, we have found that theoretically calculated σ_{cap} using the extended ℓ-summed Wong model improves with the incorporation of β_4 and corresponding cold optimum orientations at below- and near-barrier energies, whereas for above-barrier energies hot optimum orientation is preferable.

On the basis of this result, the application of θ_{opt} defining the elongated and compact configurations of β_4 deformed fragments, decaying from SHN (i.e., $^{286}Cn^*$), has been analyzed in terms of the fragmentation structure using collective clusterization approach. As a result, the symmetric fission fragments (i.e., $^{143}Ba + ^{143}Ba$) possessing the higher-order deformation are found to minimize the fragmentation potential. Experimentally, it has been noticed that fragment Ba (barium) possesses extra stability, and we have also noticed this in our theoretical calculations.

In conclusion, the application of θ_{opt} related to $\beta^{\pm}_4$ deformed actinide targets shows their significant relevance in the production as well as exit channel of superheavy nuclei (SHN). Besides, the present work raises questions regarding the collective influence of higher-order deformation in the decay products of SHN, and their stability and structural properties in reference to the spherical, quadrupole, and octupole deformed fragments. Such theoretical investigations will help in future experiments related to the higher-order deformed actinides, which participate in the fusion-fission dynamics of superheavy nuclei.

ACKNOWLEDGMENTS

The research projects of the Science and Engineering Research Board (SERB), Files No. CRG/2021/001229 and No. CRG/2021/001144, are gratefully acknowledged.

[1] V. I. Zagrebaev, Y. Aritomo, M. G. Itkis, Y. T. Oganessian, and M. Ohta, Phys. Rev. C **65**, 014607 (2001).
[2] A. Sobiczewski and K. Pomorski, Prog. Part. Nucl. Phys. **58**, 292 (2007).
[3] A. Sobiczewski, Z. Patyk, and S. Ćwiok, Phys. Lett. B **224**, 1 (1989).
[4] Y. T. Oganessian, A. Sobiczewski, and G. M. Ter-Akopian, Phys. Scr. **92**, 023003 (2017).
[5] X.-Q. Wang, X.-X. Sun, and S.-G. Zhou, Chin. Phys. C **46**, 024107 (2022).
[6] Y. Oganessian, J. Phys.: Conf. Ser. **337**, 012005 (2012).
[7] K. Chapman, Philos. Trans. R. Soc. A **378**, 20190535 (2020).
[8] N. Wang, E.-G. Zhao, and W. Scheid, Phys. Rev. C **89**, 037601 (2014).
[9] S. Hofmann, Radiochim. Acta **99**, 405 (2011).
[10] T. Ichikawa, A. Iwamoto, P. Möller, and A. J. Sierk, Phys. Rev. C **71**, 044608 (2005).
[11] Y. T. Oganessian, V. K. Utyonkov, Y. V. Lobanov, F. S. Abdullin, A. N. Polyakov, R. N. Sagaidak, I. V. Shirokovsky, Y. S. Tsyganov, A. A. Voinov, G. G. Gulbekian, S. L. Bogomolov, B. N. Gikal, A. N. Mezentsev, S. Iliev, V. G. Subbotin, A. M. Sukhov, K. Subotic, V. I. Zagrebaev, G. K. Vostokin, M. G. Itkis *et al.*, Phys. Rev. C **74**, 044602 (2006).
[12] N. Wang, J.-Q. Li, and E.-G. Zhao, Phys. Rev. C **78**, 054607 (2008).
[13] R. Smolańczuk, Phys. Rev. C **59**, 2634 (1999).
[14] A. S. Umar, V. E. Oberacker, J. A. Maruhn, and P.-G. Reinhard, Phys. Rev. C **81**, 064607 (2010).
[15] V. Y. Denisov and S. Hofmann, Phys. Rev. C **61**, 034606 (2000).
[16] V. K. Utyonkov, N. T. Brewer, Y. T. Oganessian, K. P. Rykaczewski, F. S. Abdullin, S. N. Dmitriev, R. K. Grzywacz, M. G. Itkis, K. Miernik, A. N. Polyakov, J. B. Roberto, R. N. Sagaidak, I. V. Shirokovsky, M. V. Shumeiko, Y. S. Tsyganov, A. A. Voinov, V. G. Subbotin, A. M. Sukhov, A. V. Sabelnikov,

G. K. Vostokin, J. H. Hamilton, M. A. Stoyer, and S. Y. Strauss, Phys. Rev. C **92**, 034609 (2015).
[17] Y. T. Oganessian, V. K. Utyonkov, Y. V. Lobanov, F. S. Abdullin, A. N. Polyakov, I. V. Shirokovsky, Y. S. Tsyganov, G. G. Gulbekian, S. L. Bogomolov, B. N. Gikal, A. N. Mezentsev, S. Iliev, V. G. Subbotin, A. M. Sukhov, O. V. Ivanov, G. V. Buklanov, K. Subotic, M. G. Itkis, K. J. Moody, J. F. Wild, N. J. Stoyer, M. A. Stoyer, and R. W. Lougheed, Phys. Rev. C **62**, 041604 (2000).
[18] Y. T. Oganessian, V. K. Utyonkov, Y. V. Lobanov, F. S. Abdullin, A. N. Polyakov, I. V. Shirokovsky, Y. S. Tsyganov, G. G. Gulbekian, S. L. Bogomolov, B. N. Gikal, A. N. Mezentsev, S. Iliev, V. G. Subbotin, A. M. Sukhov, G. V. Buklanov, K. Subotic, M. G. Itkis, K. J. Moody, J. F. Wild, N. J. Stoyer, M. A. Stoyer, and R. W. Lougheed, Phys. Rev. Lett. **83**, 3154 (1999).
[19] M. J. Rhoades-Brown, V. E. Oberacker, M. Seiwert, and W. Greiner, Z. Phys. A: At. Nucl. **310**, 287 (1983).
[20] H. Sharma, S. Jain, R. Kumar, and M. K. Sharma, Eur. Phys. J. A **59**, 71 (2023).
[21] R. G. Stokstad, Y. Eisen, S. Kaplanis, D. Pelte, U. Smilansky, and I. Tserruya, Phys. Rev. C **21**, 2427 (1980).
[22] B. Sharifi and D. Naderi, Nucl. Phys. A **991**, 121616 (2019).
[23] G. Giardina, S. Hofmann, A. I. Muminov, and A. K. Nasirov, Eur. Phys. J. A **8**, 205 (2000).
[24] R. K. Gupta, M. Balasubramaniam, R. Kumar, N. Singh, M. Manhas, and W. Greiner, J. Phys. G: Nucl. Part. Phys. **31**, 631 (2005).
[25] K. Hagino, Phys. Rev. C **98**, 014607 (2018).
[26] G. Adamian, N. Antonenko, W. Scheid, and V. Volkov, Nucl. Phys. A **633**, 409 (1998).
[27] L. Zhu, W.-J. Xie, and F.-S. Zhang, Phys. Rev. C **89**, 024615 (2014).
[28] A. Iwamoto, P. Möller, J. R. Nix, and H. Sagawa, Nucl. Phys. A **596**, 329 (1996).
[29] Z.-H. Liu and J.-D. Bao, Chin. Phys. C **28**, 842 (2004).
[30] G. Kaur, K. Sandhu, and M. K. Sharma, Nucl. Phys. A **971**, 95 (2018).
[31] R. G. Stokstad, Y. Eisen, S. Kaplanis, D. Pelte, U. Smilansky, and I. Tserruya, Phys. Rev. Lett. **41**, 465 (1978).
[32] X. J. Bao, S. Q. Guo, H. F. Zhang, and J. Q. Li, J. Phys. G: Nucl. Part. Phys. **43**, 125105 (2016).
[33] G. G. Adamian, N. V. Antonenko, and V. V. Sargsyan, Phys. Rev. C **79**, 054608 (2009).
[34] R. Kumar, K. Sandhu, M. K. Sharma, and R. K. Gupta, Phys. Rev. C **87**, 054610 (2013).
[35] H. C. Manjunatha, Y. S. Vidya, P. S. D. Gupta, N. Manjunatha, N. Sowmya, L. Seenappa, and T. Nandi, J. Phys. G: Nucl. Part. Phys. **49**, 125101 (2022).
[36] G. Kaur and M. K. Sharma, Commun. Theor. Phys. **72**, 025302 (2020).
[37] J. Hong, G. Adamian, N. Antonenko, P. Jachimowicz, and M. Kowal, Phys. Lett. B **809**, 135760 (2020).
[38] R. K. Gupta, M. Manhas, and W. Greiner, Phys. Rev. C **73**, 054307 (2006).
[39] G. Adamian and N. Antonenko, Eur. Phys. J. A **58**, 111 (2022).
[40] S. Jain, M. K. Sharma, and R. Kumar, Phys. Rev. C **101**, 051601(R) (2020).
[41] V. Sargsyan, G. Adamian, N. Antonenko, W. Scheid, and H. Zhang, Eur. Phys. J. A **47**, 1 (2011).
[42] V. Y. Denisov and N. Pilipenko, Phys. At. Nucl. **73**, 1152 (2010).
[43] K. Nishio, S. Hofmann, F. P. Heßberger, D. Ackermann, S. Antalic, Y. Aritomo, V. F. Comas, C. E. Düllmann, A. Gorshkov, R. Graeger, K. Hagino, S. Heinz, J. A. Heredia, K. Hirose, H. Ikezoe, J. Khuyagbaatar, B. Kindler, I. Kojouharov, B. Lommel, R. Mann, S. Mitsuoka, Y. Nagame, I. Nishinaka, T. Ohtsuki, A. G. Popeko, S. Saro, M. Schadel, A. Turler, Y. Watanabe, A. Yakushev, and A. V. Yeremin, Phys. Rev. C **82**, 024611 (2010).
[44] M. Itkis, I. Itkis, G. Knyazheva, and E. Kozulin, Nucl. Phys. A **834**, 374c (2010).
[45] K. Nishio, S. Mitsuoka, I. Nishinaka, H. Makii, Y. Wakabayashi, H. Ikezoe, K. Hirose, T. Ohtsuki, Y. Aritomo, and S. Hofmann, Phys. Rev. C **86**, 034608 (2012).
[46] H. Fink, J. Maruhn, W. Scheid, and W. Greiner, Z. Phys. **268**, 321 (1974).
[47] J. Maruhn and W. Greiner, Phys. Rev. Lett. **32**, 548 (1974).
[48] R. K. Gupta, W. Scheid, and W. Greiner, Phys. Rev. Lett. **35**, 353 (1975).
[49] A. Bohr, Dan. Mat. Fys. Medd. **26**, 14 (1952).
[50] A. N. Bohr and B. R. Mottelson, Dan. Mat. Fys. Medd. **27**, 1 (1953).
[51] D. A. Varshalovich, A. N. Moskalev, and V. K. M. Khersonskii, *Quantum Theory of Angular Momentum* (World Scientific, Singapore, 1988).
[52] P. Möller, A. Sierk, T. Ichikawa, and H. Sagawa, At. Data Nucl. Data Tables **109-110**, 1 (2016).
[53] J. Błocki, J. Randrup, W. Swiatecki, and C. Tsang, Ann. Phys. (NY) **105**, 427 (1977).
[54] R. Kumar, M. Bansal, S. K. Arun, and R. K. Gupta, Phys. Rev. C **80**, 034618 (2009).
[55] R. K. Gupta, N. Singh, and M. Manhas, Phys. Rev. C **70**, 034608 (2004).
[56] K. Sandhu, M. K. Sharma, and R. K. Gupta, Phys. Rev. C **85**, 024604 (2012).
[57] N. V. Antonenko, G. G. Adamian, W. Scheid, and V. V. Volkov, Nuovo Cimento A **110**, 1143 (1997).
[58] M. Beckerman, J. Ball, H. Enge, M. Salomaa, A. Sperduto, S. Gazes, A. DiRienzo, and J. D. Molitoris, Phys. Rev. C **23**, 1581 (1981).
[59] D. L. Hill and J. A. Wheeler, Phys. Rev. **89**, 1102 (1953).
[60] R. Dutt, A. Khare, and U. P. Sukhatme, Am. J. Phys. **59**, 723 (1991).
[61] C. Y. Wong, Phys. Rev. C **86**, 064603 (2012).
[62] S. Jain, R. Kumar, S. K. Patra, and M. K. Sharma, Phys. Rev. C **105**, 034605 (2022).
[63] R. K. Gupta, in *Clusters in Nuclei: Volume 1* (Springer, Berlin, 2010), p. 223.
[64] D. Jain, R. Kumar, and M. K. Sharma, Phys. Rev. C **87**, 044612 (2013).
[65] W. D. Myers and W. J. Swiatecki, Nucl. Phys. **81**, 1 (1966).
[66] N. Davidson, S. Hsiao, J. Markram, H. Miller, and Y. Tzeng, Phys. Lett. B **315**, 12 (1993).
[67] S. DeBenedetti, *Nuclear Interactions* (John Wiley & Sons, New York, 1964).
[68] K. Le Couteur and D. Lang, Nucl. Phys. **13**, 32 (1959).
[69] A. Bezbakh, T. Shneidman, G. Adamian, and N. Antonenko, Eur. Phys. J. A **50**, 97 (2014).

[70] K. Nishio, S. Hofmann, F. Heßberger, D. Ackermann, S. Antalic, V. Comas, Z. Gan, S. Heinz, J. Heredia, H. Ikezoe *et al.*, Eur. Phys. J. A **29**, 281 (2006).
[71] D. Jain, M. K. Sharma, Rajni, R. Kumar, and R. K. Gupta, Eur. Phys. J. A **50**, 155 (2014).
[72] Y.-S. Chen, Y. Sun, and Z.-C. Gao, Phys. Rev. C **77**, 061305(R) (2008).
[73] A. Kaur, N. Sharma, and M. K. Sharma, Phys. Rev. C **103**, 034618 (2021).
[74] G. Scamps and C. Simenel, Nature (London) **564**, 382 (2018).